First Direct Measurement of ^{22}Mg$(\alpha,p)^{25}$Al and Implications for X-Ray Burst Model-Observation Comparisons

J. S. Randhawa,[1,2,*] Y. Ayyad,[1,†] W. Mittig,[1,3] Z. Meisel,[4] T. Ahn,[5] S. Aguilar,[5] H. Alvarez-Pol,[6] D. W. Bardayan,[5] D. Bazin,[1] S. Beceiro-Novo,[3] D. Blankstein,[5] L. Carpenter,[1] M. Cortesi,[1] D. Cortina-Gil,[6] P. Gastis,[7,2] M. Hall,[5] S. Henderson,[5] J. J. Kolata,[5] T. Mijatovic,[1,8] F. Ndayisabye,[1] P. O'Malley,[5] J. Pereira,[1] A. Pierre,[1] H. Robert,[1] C. Santamaria,[1,9] H. Schatz,[1,2,3] J. Smith,[1] N. Watwood,[1] and J. C. Zamora[1,10]

[1]*National Superconducting Cyclotron Laboratory, Michigan State University, East Lansing, Michigan 48824, USA*
[2]*Joint Institute for Nuclear Astrophysics—Center for the Evolution of the Elements, Michigan State University, East Lansing, Michigan 48824, USA*
[3]*Department of Physics and Astronomy, Michigan State University, East Lansing, Michigan 48824-1321, USA*
[4]*Institute of Nuclear and Particle Physics, Department of Physics and Astronomy, Ohio University, Athens, Ohio 45701, USA*
[5]*Department of Physics, University of Notre Dame, Notre Dame, Indiana 46556-5670, USA*
[6]*IGFAE, Universidade de Santiago de Compostela, E-15782 Santiago de Compostela, Spain*
[7]*Department of Physics, Central Michigan University, Mount Pleasant, Michigan 48859, USA*
[8]*Ruđer Bošković Institute, HR-10002 Zagreb, Croatia*
[9]*Nuclear Science Division, Lawrence Berkeley National Laboratory, Berkeley, California 94720, USA*
[10]*Instituto de Fisica, Universidade de Sao Paulo, 05508-090 Sao Paulo, Brazil*

(Received 29 January 2020; revised 3 May 2020; accepted 6 October 2020; published 10 November 2020)

Type-I x-ray bursts can reveal the properties of an accreting neutron star system when compared with astrophysics model calculations. However, model results are sensitive to a handful of uncertain nuclear reaction rates, such as ^{22}Mg(α, p). We report the first direct measurement of ^{22}Mg(α, p), performed with the Active Target Time Projection Chamber. The corresponding astrophysical reaction rate is orders of magnitude larger than determined from a previous indirect measurement in a broad temperature range. Our new measurement suggests a less-compact neutron star in the source GS1826-24.

DOI: 10.1103/PhysRevLett.125.202701

Type-I x-ray bursts (XRBs) are thermonuclear explosions on the surface of accreting neutron stars powered by nuclear burning [1–3]. In recent years, advances in XRB observations and modeling have opened a unique window to constrain the neutron star mass-radius relation and other underlying physics through comparisons between observations and models [4,5]. As XRB light curves are powered by nuclear reactions, XRB models are sensitive to various nuclear physics inputs (e.g., nuclear reaction rates) [6,7]. Models with reliable nuclear physics data are needed to validate the assumptions of astrophysical models through model-observation comparisons [8]. Accurate nuclear physics input plays an equally important role in predicting the burst ashes, which alter the composition of the crust of the neutron star. In mass-accreting systems, this crust is made in part or entirely out of XRB ashes. Various sensitivity studies conducted over years have shown that the ^{22}Mg$(\alpha, p)^{25}$Al reaction rate is among the most significant reactions that directly impact light curves and burst ashes [6,7,9]. In a recent study, performed to assess the impact of uncertainties in nuclear inputs on the extraction of the neutron star mass-radius relation, the ^{22}Mg$(\alpha, p)^{25}$Al reaction rate was shown to have a significant effect even when decreased by factor 10 [8].

Prior to an XRB, accreted hydrogen is compressed and burned via the hot CNO cycles, until the triple-α reaction is initiated and the thermonuclear runaway ensues. At this point the burst begins and the temperature rises rapidly. At temperatures around 0.5–0.6 GK, breakout from the hot CNO cycle via ^{15}O$(\alpha,\gamma)^{19}$Ne and ^{18}Ne$(\alpha, p)^{21}$Na becomes efficient. These breakout reactions are crucial as it takes the flow from hot CNO cycles to higher mass region. These breakout reactions open the door for the αp process, enabling the reaction flow to reach ^{22}Mg. At this branching point, ^{22}Mg$(\alpha, p)^{25}$Al competes with the rather slow β^+ decay and with ^{22}Mg$(p,\gamma)^{23}$Al [4,10]. The current experimental constraint on this reaction rate comes from an indirect measurement where resonant states in ^{26}Si were explored through the ^{28}Si$(p, t)^{26}$Si reaction by Matic *et al.* [11]. This experimentally constrained reaction rate is more than a factor of 100 below Hauser-Feshbach (HF) predictions in the relevant XRB temperature range above 0.7 GK. The large deviation from the HF based model calculations was attributed to the lack of resonance data above 10 MeV excitation energy in ^{26}Si [11]; therefore their rate was considered to be a lower limit, and the HF based rate an upper limit. These two rates lead to significantly different results when used in XRB model calculations

resulting in a significant uncertainty of model-observation comparisons. Since XRB ashes ultimately set the composition of the accreted neutron star crust, the discrepant ash results may also impact model-observation comparisons for neutron star crust cooling [4,12,13]. Therefore, it is important to directly measure this reaction to reduce this very large uncertainty and constrain the XRB model calculations. In this work, we report the first direct measurement of the ^{22}Mg$(\alpha, p)^{25}$Al reaction using the Active-Target Time Projection Chamber (AT-TPC).

The ^{22}Mg$(\alpha, p)^{25}$Al measurement was carried out at the National Superconducting Cyclotron Laboratory. ^{22}Mg was produced from the fragmentation of a ^{24}Mg primary beam accelerated by the coupled cyclotrons and selected by the A1900 fragment separator [14]. The ^{22}Mg fragments were stopped in a linear gas cell and transported to an electron beam ion source, where their charge state increased to 12^+. Finally, the ions were injected into the ReA3 reaccelerator, accelerated to ~5 MeV/u with an average beam intensity of ~900 pps. A pure ^{22}Mg beam was delivered to the experiment station where it was first transported through a thin ionization chamber filled with isobutane at 10 torr. An ionization chamber recorded the beam intensity and identified beam contaminants [15]. Before the beam entered the active volume of the AT-TPC, it went through a 3.6-μm-thick aluminized para-aramid window of 1 cm diameter. The energy loss in the entrance window was 4.7 MeV. The AT-TPC active volume is a cylinder of length 1 m and of a radius 29.2 cm, placed in a uniform 1.9 T magnetic field generated by a solenoidal magnet. The AT-TPC was filled with 600 torr $\mathrm{He{:}CO_2}(95\%{:}5\%)$ to stop the beam in the middle. The sensor plane consists of a mosaic of 10240 equilateral triangle pads that provides x and y information of the tracks of the particles. Ionization electrons drift time provides the longitudinal component of the track. Typical drift times through the detector were around 40 μs. The ionization chamber signal was used to retain the arrival of beam particles through the window as a time reference, which is pivotal to determine the reaction vertex position along the beam axis. The AT-TPC is equipped with a hierarchical digital data acquisition system. At the bottom of this hierarchy is the AGET chip, which controls the sampling and shaping of the signals and compares them to a threshold to generate a channel level trigger. Each AGET outputs a multiplicity signal which is derived from the number of channels that are above a preset threshold amplitude. Multiplicities from each AGET (ASIC for General Electronics for TPCs) are further collected by their controlling CoBos (concentration boards) to produce a CoBo-level multiplicity signal [16]. In addition, a logical trigger signal from the ion chamber is delayed and put in coincidence with a large window opened by the CoBo multiplicity trigger. If the delayed ion chamber signal falls within this time window, a trigger signal will be generated. The AT-TPC electronics system allows the readout and trigger attributes of each channel to be set individually [15]. Among the dominating channels open at this energy are (α,α) and (α, p). From kinematics, protons are the only particles that were emitted at backward angles, i.e., $\theta_{\mathrm{lab}} > 90°$. Therefore, protons were identified by selecting backscattered particle tracks. Another possible source of backscattered protons are fusion-evaporation reactions on carbon and oxygen. Any background contribution from reactions on carbon in this angular domain were estimated (using PACE4 [17]) to be less than 0.4%. The backscattered proton tracks were analyzed using the random sample consensus (RANSAC) method [18,19]. Figure 1 shows an example of a proton track in 3D (top panel). The middle and lower panels show a 2D projection of the same track on the pad plane as well as the RANSAC analysis, respectively. The RANSAC algorithm provides the best fit of the spiral to a circle and its radius. Then, we calculate the arc length starting between the point of closest approach, which in this case is the very first point of the track (isolated using our clustering algorithm) and each point of the hit pattern. From the arc length versus z-vertex plot [Fig. 1(c)] we can extract the angle and the interaction vertex. Tracks for the (α, p) reaction channel were simulated using the AT-TPC simulation package. The AT-TPC simulation uses the virtual Monte Carlo package which relies on the GEANT4 engine. The amount of primary ionization is estimated by dividing the energy lost by the tracked particle in each time step of the simulation. The energy loss in the gas is converted into electrons that are drifted to the pad plane which also takes into account lateral and longitudinal diffusion of the ionization electrons. Pulses are generated taking into account the response function of the pad and the electronics [15]. The data are then transformed into a three-dimensional hit pattern that represents the position of each simulated interaction point convoluted with the size of the pads and the sampling rate of the electronics. More about the AT-TPC simulation package and digitization can be found in Ayyad *et al.* [18]. Simulated tracks were also analyzed as described above. The top panel of Fig. 2 shows the event-by-event reaction vertex as a function of laboratory angle for the experimental and simulated data. It is evident from the plot that the experimentally accessible angular domain is limited from 90° to 130° in the laboratory frame and agrees with the simulated data. As we are analyzing only the backscattered protons, the higher angles are accessible only when the reaction vertex is at some distance from the entrance window. The detected angular range during the experiment depends on the geometrical acceptance of the detector and the threshold of the multiplicity trigger. Figure 2(b) shows the simulated acceptance as a function of laboratory angle without and with multiplicity threshold. The inset of Fig. 2(b) shows the number of pads hit as function of the laboratory angle. It is worth pointing out that the geometrical acceptance of the detector covers up to 160°

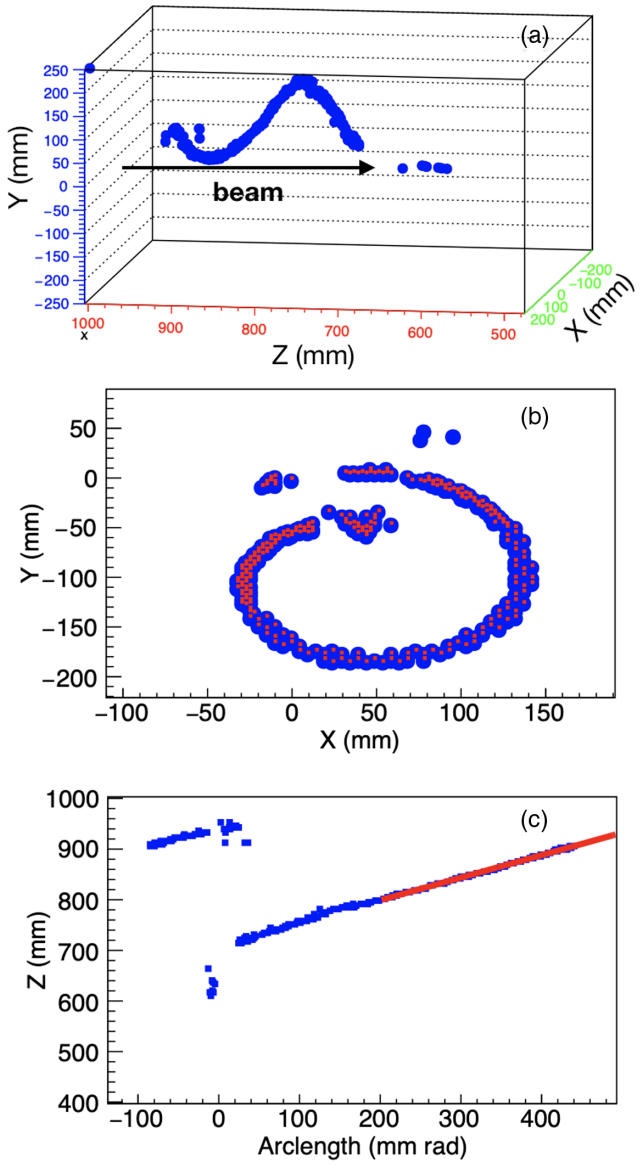

FIG. 1. Panel (a) shows a three-dimensional view of an example proton track and the arrow shows the beam direction. Panel (b) shows the projection of a proton track on the pad plane where blue dots are data points and red indicates the data points chosen for RANSAC analysis. Panel (c) shows the arclength of each hit pattern point as a function of the z coordinate. The red line is the least-squares fit performed to extract the scattering angle from the slope.

(red dots). The experimental data (blue triangles) show a sharp cutoff at ~80 hits per event. Higher laboratory angles were cut off due to this multiplicity threshold in the current experiment. To obtain the angle-integrated cross sections, the proton distribution in the laboratory frame was calculated at different beam energies using PACE4 [17]. The ratio of counts from 0° to 180° to counts in the angular region covered in this study are shown in Fig. 2(c). This energy-dependent ratio was used to obtain the angle-integrated cross section.

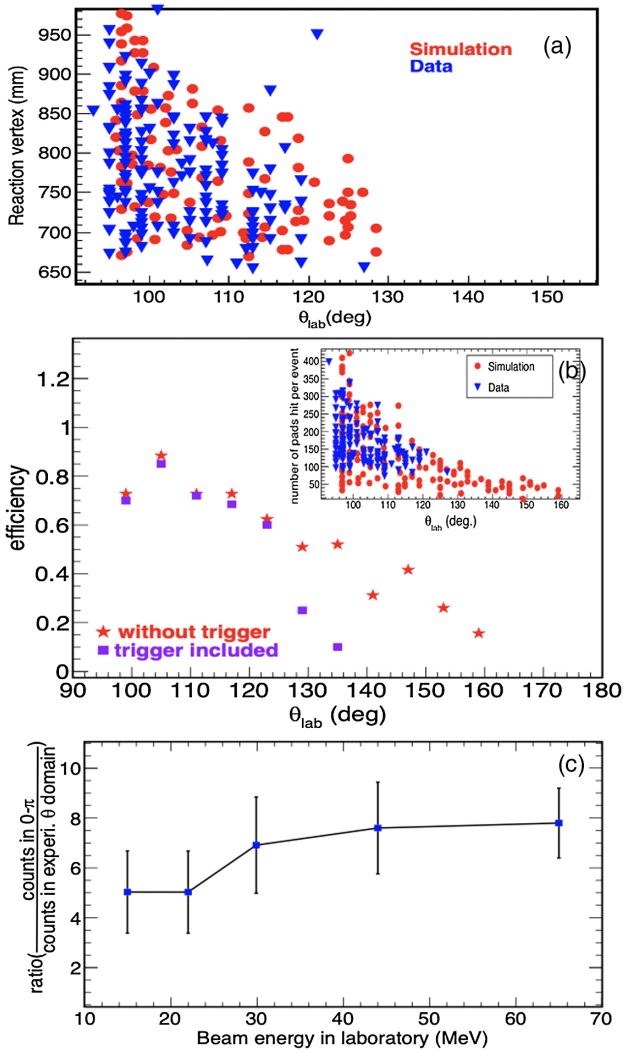

FIG. 2. Panel (a) shows the reaction vertex as a function of laboratory angle for experimental data (blue inverted triangle) overlaid on simulation data (red filled circles). Panel (b) shows the efficiency as a function of laboratory angle and the inset shows the number of pads hit per event as a function of the laboratory angle. Panel (c) shows the ratio of calculated (using PACE4) total counts over the counts in the experimental angular domain as a function of the beam energy.

The obtained excitation function is shown in Fig. 3(a) (and also in tabular form in Table I) in comparison to HF calculations. Data points are shown at the weighted energy. Here, the weighted energy is defined as $\int \sigma(E) E dE / \int \sigma(E) dE$, where the energy dependence of HF based NON-SMOKER cross sections was used [6]. Vertical error bars include contributions from statistical and systematic uncertainties. Systematic error bars include a 5% uncertainty in the number of target atoms based on energy loss tables uncertainties, 5% in the incident beam counts, and 35% error when accounting for counts outside the angular domain covered in this study. Our estimation of 35% uncertainty is based on any uncertainty originating from the model

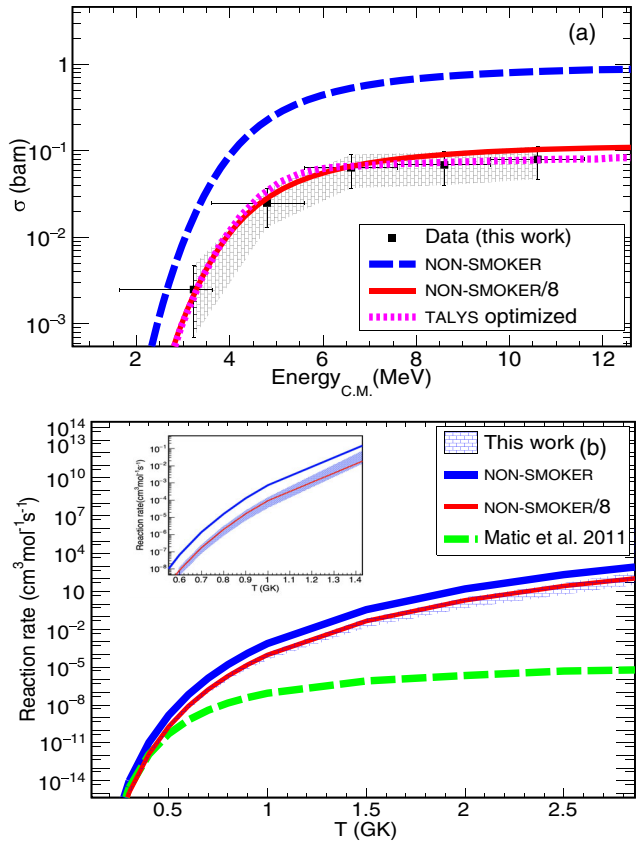

FIG. 3. Panel (a) shows the experimental cross sections obtained in the present work over a range of center-of-mass energies covered (black). For all the points, the cross section weighted energy is shown, which is the reason why horizontal error bars for the two lowest energy points are asymmetric. Panel (b) shows the reaction rate comparison of the current work to different model predictions and to the previous measurement by Matic *et al.* [11].

prediction of the proton angular distribution. Horizontal error bars reflect the bin size in center-of-mass energies. The cross sections obtained in the current work are a factor of 8–10 lower than the HF calculation results. The lowest center-of-mass energy of our measurement is located near the upper end of the astrophysical Gamow window for a 2 GK temperature [20]. Extrapolation to lower center-of-mass energies is required to obtain the cross section and reaction rate in the relevant temperature range. For this, a combination of input parameters for the TALYS code was identified to best reproduce the experimental data within error bars. In TALYS, we used the following combination of models:

TABLE I. Cross sections obtained in the present work as a function of (weighted) center-of-mass energy. Errors are shown in parentheses.

Weighted energy (MeV)	Protons detected per energy bin	Cross section (mb)	Error (stat, syst)
3.2	3	$2.5(^{+2.3}_{-1.8})$	$(^{2.1,0.9}_{1.6,0.9})$
4.8	18	26(12)	(6,11)
6.6	41	64(27)	(10,25)
8.6	40	69(29)	(11,26)
10.6	45	80(33)	(12,31)

semimicroscopic optical model potential, dispersive alpha optical potential from Demetriou *et al.* [21], microscopic level densities from Goriely's tables, and γ-ray strength functions from the Brink-Axel Lorentzian model [22]. The best fit to the experimental cross section was achieved after multiplying the default normalization factor for the shape of the double-folding α potential by 0.884 and the default level density of the compound nucleus by a factor of 2.60. The optimized TALYS reaction rate (this work) is shown in Fig. 3(b), lower panel, where the shaded area shows the estimated reaction rate uncertainty. The reaction rate uncertainty was estimated using the maximum and minimum cross sections obtained in this work indicated by vertical error bars and shaded regions in Fig. 3(a). The horizontal error bars in the cross-section measurement in Fig. 3(a) represents the energy range over which given cross sections are energy averaged. The astrophysical reaction rate in Fig. 3 (b) is energy averaged and hence does not reflect the effect of horizontal error bars of Fig. 3(a). The dramatic disagreement between the reaction rates from Matic *et al.* [11] and HF model calculations above 0.4 GK deduced in the previous measurement was not observed in the current work. Above 1 GK, the reaction rate reported in this work follows a similar trend, within the error bars, as the one inferred from NON-SMOKER but notably smaller in magnitude. With the current measurement the reaction rate in the critical temperature range around 0.7–1 GK is determined by using the best-fit TALYS model to experimental data just above the Gamow window. This new reaction rate was fit to the standard seven parameter REACLIB database form and best-fit parameters in the temperature range 0.3–3.5 GK are provided in Table II.

To assess the impact of our measurement on the XRB light curve, we performed multizone XRB calculations with the code MESA, following those described in Refs. [5,8].

TABLE II. Best-fit parameters for new rate as a fit to standard seven parameter REACLIB form, i.e., $\exp[a_0 + \sum_{i=1}^{5} a_i T_9^{(2i-5)/3} + a_6 \ln(T_9)]$.

Parameter	a_0	a_1	a_2	a_3	a_4	a_5	a_6
Best-fit value	43.939	0.0	-5.31×10	6.35×10^{-1}	-8.29×10^{-1}	6.5×10^{-2}	-6.6×10^{-1}

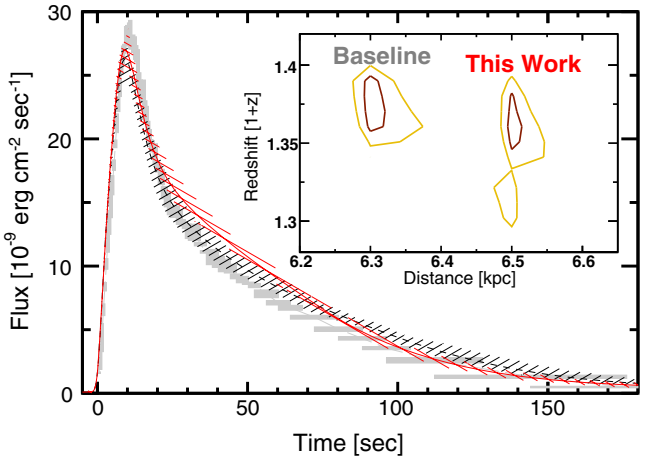

FIG. 4. XRB light curve comparison for GS1826-24 observations (gray boxes), MESA calculations using the NON-SMOKER rate for $^{22}\mathrm{Mg}(\alpha, p)$ (black band), and the NON-SMOKER rate reduced by /8 (red band). The inset shows the corresponding 68% (red) and 95% (yellow) confidence intervals for the distance and redshift, which were determined as described in Ref. [8].

We employed the REACLIBv2.2 nuclear reaction rate library, where the NON-SMOKER HF rate of Ref. [6] is the default for $^{22}\mathrm{Mg}(\alpha, p)^{25}\mathrm{Al}$. We used the astrophysical conditions that were found to best reproduce observables from the year 2000 bursting epoch of the source GS1826-24 [5,23]. Figure 4 compares MESA results to astronomical observations. We use a distance of 6.3 kpc and redshift $(1 + z)$ of 1.38, which provide the best fit between the observed light curve and our baseline calculation, to mimic the x-ray detection solid angle and neutron star surface gravitational redshift that modify the observed light curve.

Figure 4 shows that the calculations from Refs. [5,8] (black band) generally reproduce the observed light curve (gray boxes), including the recurrence time between bursts (which is not shown). However, this agreement is substantially diminished when reducing the NON-SMOKER rate for $^{22}\mathrm{Mg}(\alpha, p)$ by a factor of 8 (red band). In particular, the tail of the XRB light curve is substantially modified because a reduced $^{22}\mathrm{Mg}(\alpha, p)$ rate effectively enhances hydrogen burning early in the burst by making the path $^{22}\mathrm{Mg}(p, \gamma)^{23}\mathrm{Al}(p, \gamma)^{24}\mathrm{Si}$ [24] more competitive. Therefore, less hydrogen is available to be burned at later times following the light curve peak, resulting in a more rapid decline of the light curve tail. The implication of our result is that an alternative distance and surface gravitational redshift are needed in order to reproduce observed features of GS1826-24, as shown in the Fig. 4 inset. This implies a less-compact neutron star in GS1826-24 than determined by Ref. [8]. Our results bring constraints to an important uncertainty in XRB model calculations which will improve the extraction of neutron star compactness via XRB light curve model-observation comparisons.

The authors would like to thank the beam delivery group. This work was supported by the U.S. National Science Foundation (NSF), U.S. under Grants No. MRI-0923087 and No. PHY-140444, under Cooperative Agreement No. PHY-1565546, Grant No. PHY-1713857, and by Grant No. PHY-1430152 (JINA Center for the Evolution of the Elements), No. PHY-1102511, and No. PHY-1913554. T. A. and D. W. B. acknowledges NSF Grant No. PHY-1713857, J. J. K. acknowledges the NSF Grant No. 14-01343. P. G. would like to acknowledge the support by the College of Science and Engineering of CMU. Z. M. acknowledges the U.S. Department of Energy under Grants No. DE-FG02-88er40387 and No. DESC0019042. J. C. Z. thanks Fundação de Amparo a Pesquisa do Estado de São Paulo (FAPESP) for support under Grant No. 2018/04965-4. The authors are thankful to Domenico Santonocito (INFN) for providing the Cascade calculations.

*Corresponding author.
randhawa@nscl.msu.edu
†Corresponding author.
ayyadlim@nscl.msu.edu

[1] W. H. G. Lewin, J. van Paradijs, and R. E. Taam, X-ray bursts, Space Sci. Rev. **62**, 223 (1993).
[2] H. Schatz and K. Rehm, X-ray binaries, Nucl. Phys. **A777**, 601 (2006).
[3] J. Jose, *Stellar Explosions: Hydrodynamics and Nucleosynthesis* (CRC Press, Boca Raton, FL, 2016).
[4] Z. Meisel, A. Deibel, L. Keek, P. Shternin, and J. Elfritz, Nuclear physics of the outer layers of accreting neutron stars, J. Phys. G **45**, 093001 (2018).
[5] Z. Meisel, Consistent modeling of GS1826-24 X-ray bursts for multiple accretion rates demonstrates the possibility of constraining rp-process reaction rates, Astrophys. J. **860**, 147 (2018).
[6] R. H. Cyburt, A. M. Amthor, R. Ferguson, Z. Meisel, K. Smith, S. Warren, A. Heger, R. D. Hoffman, T. Rauscher, A. Sakharuk, H. Schatz, F. K. Thielemann, and M. Wiescher, The JINA reaclib database: Its recent updates and impact on type-I X-ray bursts, Astrophys. J. Suppl. Ser. **189**, 240 (2010).
[7] R. H. Cyburt, A. M. Amthor, A. Heger, E. Johnson, L. Keek, Z. Meisel, H. Schatz, and K. Smith, Dependence of X-ray burst models on nuclear reaction rates, Astrophys. J. **830**, 55 (2016).
[8] Z. Meisel, G. Merz, and S. Medvid, Influence of nuclear reaction rate uncertainties on neutron star properties extracted from X-ray burst model–observation comparisons, Astrophys. J. **872**, 84 (2019).
[9] A. Parikh, J. José, F. Moreno, and C. Iliadis, The effects of variations in nuclear processes on type I X-ray burst nucleosynthesis, Astrophys. J. Suppl. Ser. **178**, 110 (2008).
[10] J. L. Fisker, F.-K. Thielemann, and M. Wiescher, The nuclear reaction waiting points: 22 Mg, 26 Si, 30 S, and 34 Ar and bolometrically double-peaked type I X-ray bursts, Astrophys. J. **608**, L61 (2004).

[11] A. Matic, A. M. van den Berg, M. N. Harakeh, H. J. Wortche, M. Beard *et al.*, High-precision $^{28}Si(p,t)^{26}Si$ reaction to determine $^{22}Mg(\alpha,p)^{25}Al$ reaction rates, Phys. Rev. C **84**, 025801 (2011).

[12] Z. Meisel and A. Deibel, Constraints on Bygone nucleosynthesis of accreting neutron stars, Astrophys. J. **837**, 73 (2017).

[13] R. Lau, M. Beard, S. S. Gupta *et al.*, Nuclear reactions in the crusts of accreting neutron stars, Astrophys. J. **859**, 62 (2018).

[14] D. Morrissey, B. Sherrill, M. Steiner, A. Stolz, and I. Wiedenhoever, Commissioning the A1900 projectile fragment separator, Nucl. Instrum. Methods Phys. Res., Sect. B **204**, 90 (2003).

[15] J. Bradt, D. Bazin, F. Abu-Nimeh *et al.*, Commissioning of the active-target time projection chamber, Nucl. Instrum. Methods Phys. Res., Sect. A **875**, 65 (2017).

[16] E. Pollacco, G. Grinyer, F. Abu-Nimeh, T. Ahn, S. Anvar *et al.*, GET: A generic electronics system for TPCs and nuclear physics instrumentation, Nucl. Instrum. Methods Phys. Res., Sect. A **887**, 81 (2018).

[17] O. Tarasov and D. Bazin, LISE++: Radioactive beam production with in-flight separators, Nucl. Instrum. Methods Phys. Res., Sect. B **266**, 4657 (2008).

[18] Y. Ayyad, N. Abgrall, T. Ahn *et al.*, Next-generation experiments with the Active Target Time Projection Chamber (AT-TPC), Nucl. Instrum. Methods Phys. Res., Sect. A **954**, 161341 (2020).

[19] Y. Ayyad, W. Mittig, D. Bazin, S. Beceiro-Novo, and M. Cortesi, Novel particle tracking algorithm based on the random sample consensus model for the Active Target Time Projection Chamber (AT-TPC), Nucl. Instrum. Methods Phys. Res., Sect. A **880**, 166 (2018).

[20] T. Rauscher, Relevant energy ranges for astrophysical reaction rates, Phys. Rev. C **81**, 045807 (2010).

[21] P. Demetriou, C. Grama, and S. Goriely, Improved global α-optical model potentials at low energies, Nucl. Phys. **A707**, 253 (2002).

[22] P. Axel, Electric dipole ground-state transition width strength function and 7-MeV photon interactions, Phys. Rev. **126**, 671 (1962).

[23] D. K. Galloway, A. J. Goodwin, and L. Keek, Thermonuclear burst observations for model comparisons: A reference sample, Pub. Astron. Soc. Aust. **34**, e019 (2017).

[24] C. Wolf, C. Langer, F. Montes, J. Pereira, W. J. Ong *et al.*, Constraining the Neutron Star Compactness: Extraction of the $^{23}Al(p,\gamma)$ Reaction Rate for the rp Process,Phys. Rev. Lett. **122**, 232701 (2019).